RSC Advances

PAPER

View Article Online
View Journal | View Issue

Cite this: *RSC Adv.*, 2025, **15**, 19966

Enhancement of the electrochemical response of a V_2O_5 integrated biochar@poly(aniline–pyrrole) hybrid composite-coated graphite electrode

Md. Mahabur Rahman,[ab] Abdulla Al Mamun,[a] Hideto Minami,[c] Md. Kawsar Hossain,[b] S. Manjura Hoque,[d] Mostafa K. Sharafat[e] and Hasan Ahmad *[a]

The fabrication of sustainable electrode materials with high specific capacitance values is essential for designing energy-efficient supercapacitors. With this aim, herein, V_2O_5-integrated biochar@poly(aniline–pyrrole), named the BC@CCp@V_2O_5 hybrid composite, is evaluated as an electrode material. First, biochar (BC) is prepared *via* a simple hydrothermal treatment of sucrose solution. Then, conducting poly(aniline–pyrrole) (CCp) is incorporated *via* a seeded chemical oxidation method to yield BC@CCp composite particles. Finally, the BC@CCp composite is thoroughly blended with calcined V_2O_5 at a composite to V_2O_5 (w/w) ratio of 4 : 1. The morphology and surface composition of the BC@CCp@V_2O_5 hybrid composite are analyzed and confirmed *via* electron microscopy and various spectral analyses. The electrochemical properties of BC@CCp, calcined V_2O_5 and the BC@CCp@V_2O_5-coated graphite electrode are measured and compared. According to galvanostatic charge discharge (GCD) measurements, the BC@CCp@V_2O_5-coated electrode shows an exceptionally high capacitance value of 4150.6 F g^{-1} at a current density of 1.0 A g^{-1}. The BC@CCp@V_2O_5-coated electrode also demonstrates excellent capacitance retention (134%) at 10.0 A g^{-1} after 1000 charge–discharge cycles. This significant enhancement in the capacitance and stability is achieved owing to the combination of the individual components' properties and the synergistic interplay between calcined V_2O_5 and the active centers of BC@CCp. These observations represent a significant advancement in the design of sustainable BC@CCp@V_2O_5 electrode materials for application in energy-efficient supercapacitor devices.

Received 12th February 2025
Accepted 28th May 2025

DOI: 10.1039/d5ra01022e

rsc.li/rsc-advances

1. Introduction

Scientists and engineers are showing great concern towards energy and environmental problems, which has encouraged them to develop sustainable, eco-friendly energy future and energy-storage facilities. Among the energy storage facilities, electrochemical capacitors have attracted considerable attention because of their low ohmic equivalent series resistance, fast and reversible charge–discharge capability, high specific capacitance, high power density, high cycle stability, minimum maintenance costs and green technology.[1–3] Supercapacitors are promising in developing a wide range of items, including electronic devices, uninterruptible power supplies (UPSs), fuel cell vehicles, electric vehicles and large-scale smart electric grids. Supercapacitors are of two types based on their energy storage mechanisms. One type is electrical double-layer capacitors (EDLCs), which store energy *via* the adsorption–desorption of electrostatic ions at the electrode–electrolyte interface. The other is pseudocapacitors (PCs), which store energy through quick and reversible faradaic redox reactions occurring at the subsurface of electrode materials.[4,5] Generally, PC electrode materials made from conducting polymers and metal oxides possess superior specific capacitances than EDLC electrode materials (*e.g.*, carbon-rich materials). Therefore, the combination of EDLC and PC materials will afford hybrid supercapacitor electrode materials with extraordinary charge storage capacities and high cycle stability and energy density.

Biochar (BC), a carbon-rich material, is a potential environment-friendly EDLC electrode material. Additionally, the regulation of the surface area, morphology and functionality of BC enables the design of numerous materials for applications in soil reclamation and energy storage and as adsorbents, catalysts, and supports for catalysts.[6–12] However, the native BC electrode is not suitable for fabricating high energy storage

[a]*Research Laboratory of Polymer Colloids and Nanomaterials, Department of Chemistry, Rajshahi University, Rajshahi 6205, Bangladesh. E-mail: hahmad@ru.ac.bd; samarhass@yahoo.com*

[b]*Department of Chemistry, Pabna University of Science and Technology, Pabna 6600, Bangladesh*

[c]*Graduate School of Engineering, Kobe University, Kobe 657-8501, Japan*

[d]*Materials Science Division, Bangladesh Atomic Energy Commission, Dhaka, Bangladesh*

[e]*Department of Chemistry, Begum Rokeya University, Rangpur-5400, Bangladesh*

devices because of its poor electrical conductivity, initial faradaic losses and swelling during cell reactions.[13] Therefore, it has become mandatory to enhance the efficiency of BC-derived electrode materials through chemical modification. It has already been proven that conducting polymers, such as pyrrole (Py), aniline (Ani) and thiophene (PTh), containing π-conjugated double bonds can enhance redox reactions and charge-storage capacities.[14–16] For example, BC combined with a conducting polymer and a metal oxide can generate electrode materials with a high energy storage capacity.[12,16] The strong compatibility of carbon-rich BC with conducting polymers as well as the bonding of metal oxides with the electron-rich heteroatom of conducting polymers can introduce strong synergistic interactions among the individual components for stable composite formation. Hence, the designed materials will have a conducting backbone with improved electrical conductivity.[17] Furthermore, the strong synergistic interaction will prevent the destruction of the conducting polymer backbone after repeated inclusion and exclusion of counter ions during the redox reactions. In return, the fabricated BC/conducting polymer/metal oxide hybrid composite will exhibit good cyclability, electrical conductivity, mechanical stability and distinct redox reactions when used as electrode materials in energy storage devices.

So far, different types of metal oxides, *e.g.*, Y_2O_3, ZnO, CoO, SnO_2, NiO, CeO_2, WO_3, Fe_3O_4, TiO_2, and V_2O_5, have been employed for preparing conducting polymer composites, and some have been tested for supercapacitor applications.[16,18–26] Among these metal oxides, vanadium pentoxide (V_2O_5) shows promising properties for supercapacitor applications, including high theoretical capacitance, different oxidation states (V^{2+}, V^{3+}, V^{4+} and V^{5+}), relatively low prices, multilayered structures and acceptable toxicity.[27,28] Based on these advantages of V_2O_5, a mechanical approach for its integration into BC-supported conducting polymers is developed in this study. In some research studies, the improvement in the performance of carbon/V_2O_5 composites used as supercapacitor electrodes has already been discussed. For example, Saravanakumar *et al.* designed carbon-coated V_2O_5 (C@V_2O_5) and reported a higher capacitance, a superior rate capacity, lower charge transfer hindrance and better capacitance retention.[29] Li *et al.* created abundant oxygen vacancies in a V_2O_{5-x}@carbon cathode *via* the plasma-enhanced chemical vapor deposition method for applications in high-energy-density aqueous zinc-ion batteries.[30] Zhang *et al.* observed the enhancement in the specific capacitance of the 3D porous network structure of reduced graphene oxide/V_2O_5 caused by better electron transfer between the electrode and electrolyte.[31] Lee *et al.* also observed an improvement in the specific capacitance, energy density and cycle stability of a graphene/V_2O_5 composite electrode.[32] Identical observations were also reported for other carbon materials including carbon nanotubes and multiwalled carbon nanotubes.[33–35] Very recently, Vishwakarma *et al.* observed a significant improvement in the specific capacitance (737 F g^{-1} at 1 A g^{-1}) of a 10% graphene-oxide-doped V_2O_5 nanocomposite electrode prepared under microwave irradiation.[36] Some researchers have studied the integration of V_2O_5 with conducting polymers for energy storage applications. Shao *et al.* used the layer-by-layer technique to assemble hybrid electrodes comprising PAni-V_2O_5 and observed the electrochemical response from both components.[37] Wang and his group prepared a PPy-encapsulated V_2O_5 nanowire membrane and observed higher supercapacitive performance.[38] Tong *et al.* developed a core-shell-type V_2O_5/PAni nanofiber and found a synergistic improvement in the electron transport and mechanical properties for energy storage.[39] Li *et al.* intercalated conductive poly(3,4-ethylenedioxythiophene) into V_2O_5 for enhancing the electron transport property and structural stability in zinc-ion batteries.[40] Bi *et al.* improved the electrochemical performance *via* the generation of oxygen vacancies in V_2O_5 coated with a conducting polymer.[41] From this literature survey, it is evident that either carbon materials or conducting polymer in combination with V_2O_5 have been investigated for composite formation and applications in supercapacitor devices. However, to date, little attention has been given to the fabrication of supercapacitor electrodes that contain carbon-rich materials, conducting polymers and V_2O_5. In only one research study, Tabrizi and his group designed PAni nanoarrays on a graphene oxide sheet using V_2O_5 and ammonium persulfate as dual oxidants.[42] They observed a significant improvement in the specific capacitance (712 F g^{-1} at 0.5 A g^{-1} in 1 M H_2SO_4).

In this study, BC@CCp@V_2O_5 (CCp stands for 'conducting Ani–Py copolymer') hybrid composite particles are prepared and evaluated for potential use as a sustainable electrode material in supercapacitors. The objective of incorporating the Ani–Py copolymer, instead of a homopolymer, is to increase the structural uniformity of copolymer chains, π-conjugation and final conductivity.[12,43] According to this investigation, it is also possible to accommodate the distinct advantages of PAni and PPy in one matrix.[44] It is important to mention that BC, a low-cost biomass, has not been studied for hosting CCp and V_2O_5. More precisely, no such three-component hybrid system, *i.e.*, V_2O_5-integrated BC@CCp, has been evaluated as an electrode material for applications in batteries. First, BC was prepared by the hydrothermal heat treatment of a sucrose solution, a comparatively safe natural material. Then, BC@CCp was obtained by the redox-initiator-activated chemical oxidation of aniline and pyrrole using BC as core particles. Finally, the final BC@CCp@V_2O_5 hybrid composite was obtained by only mechanically blending the washed and dried BC@CCp powder with the calcined V_2O_5 powder in a w/w ratio of 4 : 1. The preparation scheme is presented in Fig. 1. The composite formation was examined using electron microscopy, Fourier transform IR (FTIR) spectroscopy, X-ray diffraction (XRD) and X-ray photoelectron spectroscopy (XPS). The overall spectral and image analyses confirmed the generation of (Ani–Py) copolymer realms and the integration of V_2O_5 on the BC surface. A graphite rod was coated with the BC@CCp@V_2O_5 hybrid composite, and its electrochemical performance was compared with the respective BC@CCp composite and calcined V_2O_5-coated graphite rod. The coating of the BC@CCp@V_2O_5 hybrid composite resulted in a remarkable improvement in the specific capacitance, cycle stability and rate capacity along with

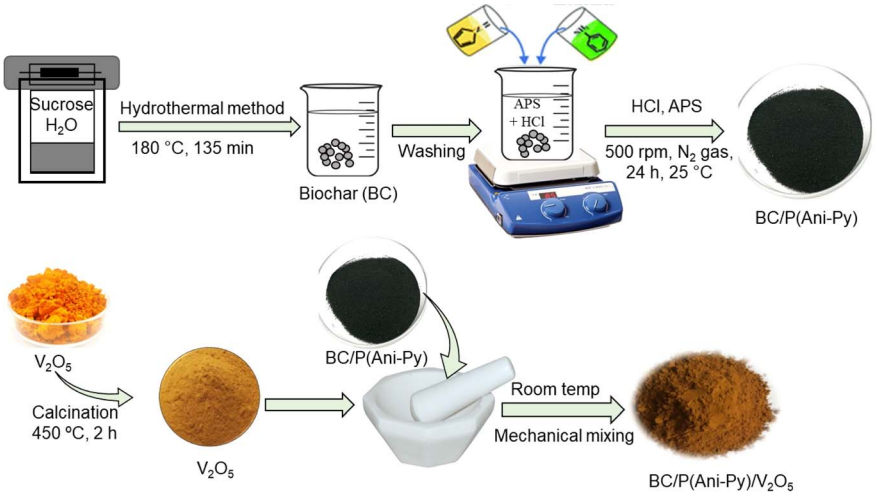

Fig. 1 Synthesis scheme for the BC@CCp@V_2O_5 hybrid composite.

a reduction in the charge transfer resistance. Specifically, the BC@CCp@V_2O_5-coated graphite electrode displayed fast charging and comparatively slow discharging, a prerequisite for energy-efficient storage devices.

2. Materials and method

2.1. Materials

Monomer-grade aniline and pyrrole and reagent-grade sucrose, procured from Sigma-Aldrich Chemie GmbH, USA, were used as received. Analytical-grade V_2O_5 was purchased from Merck, India, for preparing the hybrid composite. Ammonium persulfate ($(NH_4)_2S_2O_8$) and HCl from Merck, India, were utilized as the oxidant and dopant, respectively. The non-ionic Triton X-405 surfactant, purchased from Sigma-Aldrich Chemie GmbH, USA, was used to stabilize the composite suspension. KCl (Merck, India) was used as the electrolyte during electrochemical analysis. The polyvinylidene fluoride (PVDF) binder and *N*-methyl-2-pyrrolidone (NMP), procured from Sigma-Aldrich Chemie GmbH, USA, were employed to coat the graphite working electrode. Distilled deionized (DD) water was collected from a water purification unit (Puricom, Taiwan) installed in the department.

2.2. Preparation of BC core particles

A suspension of BC core particles was obtained *via* the hydrothermal treatment of a sucrose solution, according to our previous study.[12] In detail, 100 mL of a sucrose solution (0.8 M) in DD water was taken in a Teflon-lined stainless-steel reactor. The reactor was heated to 180 °C in an oven for 135 min. The black BC particles were isolated by centrifugation (6000 rpm) and repeatedly cleaned using DD water until the supernatant became clear.

2.3. Preparation of BC@CCp composite particles

The electroactive BC@CCp composite particles were prepared *via* the *in situ* chemical oxidation method. According to our previous study, a weight ratio of 1 : 1 for BC to the mixed monomer was selected for the composite preparation.[12] Aniline and pyrrole contents in the monomer mixture were identical on a weight basis. BC core particles (1.0 g), requisite amounts of each monomer (total 1.0 g) and Triton X-405 were taken in a glass reactor containing 50 mL of 0.1 M HCl. The reactant mixture was thoroughly stirred on a magnetic stirrer at 500 rpm to form a homogeneous dispersion. After temperature equalization at 25 °C, an aqueous $(NH_4)_2S_2O_8$ (2.0 g) solution was slowly added under continuous stirring. The oxidative copolymerization started immediately. The reaction was continued for 24 h in a N_2 atmosphere, and the pH was controlled near 1.0. The black BC@CCp composite particles were cleaned *via* repeated washing with DD water till the remaining dispersion medium became transparent.

2.4. Preparation of the BC@CCp@V_2O_5 hybrid composite

Commercial V_2O_5, taken in a platinum crucible, was transferred to a muffle furnace (Gallenkamp, Germany) connected to an external thermocouple and heated to 450 °C at a heating rate of 6 °C min^{-1}. The calcination was continued for 2 h in an air-tight condition in order to achieve higher crystallinity and capacitance values.[32] The calcined V_2O_5 powder and previously washed BC@CCp composite powder were mechanically blended in a glass mortar equipped with a hand pestle for approximately 20 min at 25 °C to obtain an almost-homogeneous powdered mixture. The weight ratio of BC@CCp to V_2O_5 was maintained at 4 : 1 during blending. The as-synthesized BC@CCp@V_2O_5 hybrid composite was characterized, and electrochemical measurements were performed without washing it.

2.5. Material characterization

The surface topography, morphology and size distribution of prepared particles were assessed by scanning electron microscopy (SEM; JSM-6510, JEOL, Tokyo, Japan) and transmission electron microscopy (TEM; JEM-1230, JEOL, Japan). FTIR spectroscopy (PerkinElmer, FTIR-100, USA) was used to examine the

changes in the surface composition during the step-wise preparation of hybrid composites. XPS (PHI X-tool, ULVAC-PHI, Inc., Japan) was employed for investigating the surface elemental composition and valence states of vanadium. During the acquisition of XPS spectra, a monochromatic Al Kα radiation (1486.6 eV) at 15 kV, 50 W and an X-ray current of 20 mA were applied. The acquisition area was 20 μm, the take-off angle was fixed at 45°, and the pressure in the measurement chamber was 8.0×10^{-7} Pa. The pass energy was fixed at 280 eV, and the step size was set at 1.0 eV. The XRD patterns of the dried samples were measured at 25 °C using an X-ray diffractometer (Bruker D8 Advance, Germany). A Cu Kα radiation (Î») of 1.5406 Å, a tube voltage of 33 kV, and a tube current of 45 mA were used for measuring diffraction intensities in 2θ values from 5° to 90° at a scanning rate of 10° min^{-1}.

2.6. Electrochemical measurements

The cyclic voltammetry (CV), galvanostatic charging–discharging (GCD), and potential electrochemical impedance spectroscopy (PEIS) measurements were carried out using a Corrtest electrochemical workstation, CS350, China. A three-electrode system was used for this purpose. The graphite rod coated with the relevant sample was used as the working electrode. At the same time, a platinum wire was used as the counter electrode, and Ag/AgCl was used as the reference electrode. All electrochemical measurements were conducted in a 1.0 M KCl electrolyte solution at 25 °C. The active segment of the graphite rod was coated/modified with a homogeneous mash of the electroactive sample and PVDF binder in a 90 : 10 weight ratio mixed in the NMP solvent. The electroactive materials used for electrode fabrication were the BC@CCp composite, calcined V_2O_5 and BC@CCp@V_2O_5 hybrid composite, respectively. The fabricated working electrode was heated to dryness at 60 °C for 12 h before electrochemical measurements. The loading of the electroactive sample was maintained in the range from 1.5 to 2.0 mg, and the electrode area was 6.15 cm^2.

In order to ensure an inert atmosphere, N_2 gas was first passed through the electrolyte for 10 min. The active part of the graphite electrode was immersed in the electrolyte solution. CV experiments were performed within the potential range from −0.2 to +0.6 V, and the scan rate was fixed at 50 mV s^{-1}. The effects of different scan rates (10–100 mV s^{-1}) and potential windows (−0.2 to + 1.0 V) were also studied for the BC@CCp@V_2O_5 hybrid composite-modified electrode to understand the optimal operating voltage and the effectiveness of the hybrid composite as an electrode material.

GCD experiments in the potential range from −0.2 to +0.6 V were carried out at a fixed current density of 1.0 A g^{-1} using the identical electrode after subsequent CV measurements. The effects of different current densities (1.0 to 5.0 A g^{-1}) on GCD curves were also studied for calcined V_2O_5 and BC@CCp@V_2O_5 hybrid composite-coated graphite electrodes. PEIS experiments for all three fabricated electrodes were performed in the frequency range from 5×10^{-2} to 5×10^{-5} Hz, and the scan rate was maintained at 50 mV s^{-1}. ZSimpWin software was used to process experimental PEIS data. Cycle stability tests from the GCD measurements of each fabricated graphite electrode were also performed at a current density of 10.0 A g^{-1}. The error range was calculated from three successive measurements, observed maximum of up to 2% at different points. The specific capacitance (C_s) of the respective electroactive sample was calculated from the GCD curve according to eqn (1):

$$C_s = \frac{I \times \Delta t}{m \times \Delta V} \quad (1)$$

where ΔV is the discharge potential, barring the IR drop, m is the mass (g) of the sample coated on the electrode, and I and Δt are the discharge current (A) and time (s), respectively. The energy density (E; Wh kg^{-1}) and power density (P; W kg^{-1}) of each fabricated electrode were calculated from GCD experiments using eqn (2) and (3), respectively:

$$E = \frac{C_s \times (\Delta V)^2}{2 \times 3.6} \quad (2)$$

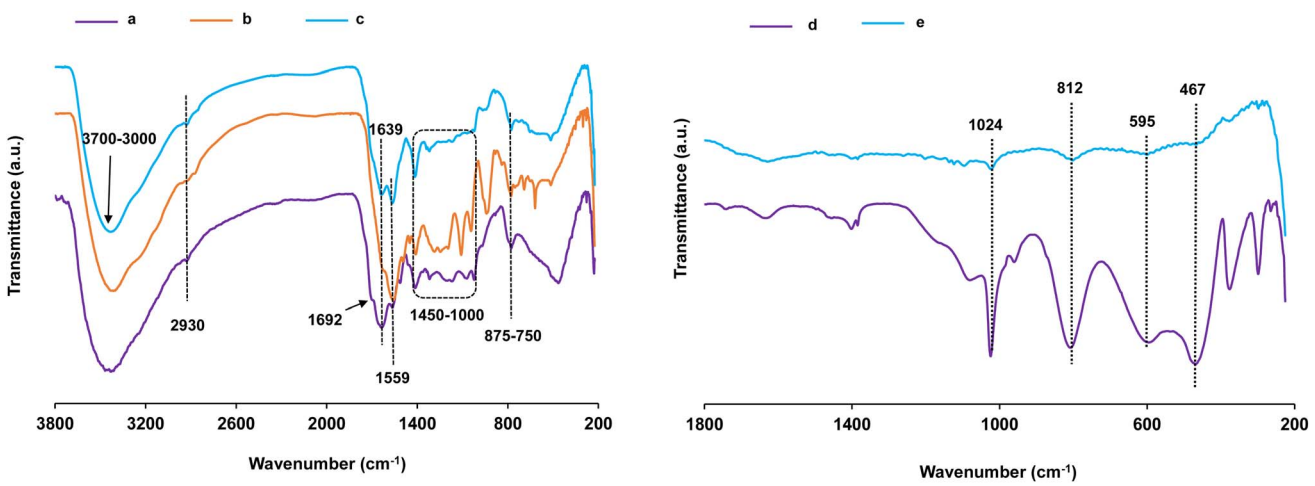

Fig. 2 FT-IR spectra of the BC core (a), CCp (b), BC@CCp composite (c), calcined V_2O_5 (d) and BC@CCp@V_2O_5 hybrid composite (e) particles recorded in KBr pellets.

$$P = \frac{E \times 3600}{\Delta t} \quad (3)$$

The capacitance retention stability (%), V_{cm} was calculated using eqn (4):

$$V_{cm} = \frac{C_s^1}{C_s^2} \times 100 \quad (4)$$

where C_s^1 and C_s^2 are the specific capacitances in the first and specific cycles, respectively.

3. Results and discussion

3.1. Characterization

The spectral analysis obtained from FTIR spectroscopy gives information about the surface functionality of the reaction product. A comparative plot of the FTIR spectra of the BC core, CCp, BC@CCp, calcined V_2O_5, and BC@CCp@V_2O_5 is given in Fig. 2. The spectrum of the BC core (Fig. 2a) illustrates the stretching signals at approximately 2930 and 3000–3700 cm^{-1}, attributed to aliphatic C–H and O–H (moisture) vibrations, respectively. The vibrations of the C=O group derived from carbonyl, quinone, and ester/carboxyl functionalities and the aromatic C=C functional group can be verified from the bands at 1692, 1639 and 1559 cm^{-1}, respectively.[45,46] The stretching and bending signals of C=C, C–O (ester or ether) and phenolic O–H are recognizable in the 1000–1450 cm^{-1} range.[47,48] The out-of-plane bending vibrations of the aromatic C–H group are represented by the bands in the 875–750 cm^{-1} region.[47] It is important to add that during batch-wise preparation, no significant structural change in BC was observed, as indicated by the FTIR spectra from different batches. In the spectrum of CCp (Fig. 2b), the wide bands at 1559 and 1639 cm^{-1} correspond to the quinonoid C–C stretching of the PAni block and C=C/C–C stretching of the PPy block, respectively.[44,48] They are a sign of the reaction between aniline and pyrrole during oxidative copolymerization. The absorption at 1112 cm^{-1} perhaps corresponds to the in-plane C–H bending vibration originated from substituted benzene in PAni.[48] The absorption signals averaged at 1390 and 1480 cm^{-1} can be assigned to the semiquinonoid ring (–N-ring) and benzenoid ring (C=C) stretching vibrations of PAni, respectively.[49] The intense peak for the C–C out-of-ring deformation of the PPy segment is found at 960 cm^{-1}.[50] Comparatively, the spectrum of BC@CCp composite particles (Fig. 2c) is dominated by peaks resembling the absorption signals of CCp. These comparative spectral analyses suggest that BC surface modification occurs, and the BC@CCp composite is obtained. The spectrum of the native calcined V_2O_5 powder (Fig. 2d) shows an absorption peak at 467 cm^{-1}, corresponding to the stretching of shared oxygen among three vanadium atoms, and the signal at 812 cm^{-1} corresponds to V–O–V vibrations.[51] The other highly intense absorption band at 1024 cm^{-1} signifies crystalline orthorhombic V_2O_5 and the stretching absorption modes of V=O.[38,51] The suppression of the absorption signals derived from CCp in the BC@CCp@V_2O_5 hybrid composite (Fig. 2e) indicates the possible coverage of the BC@CCp composite by V_2O_5 particles. The solid–solid interaction does not produce any noticeable red/blue shift of the characteristic absorption signals of V_2O_5.

The surface topographies and size distributions of the BC core, BC/CCp, calcined V_2O_5 and BC@CCp@V_2O_5 are confirmed from the SEM images given in Fig. 3. The almost-sphere-shaped BC core particles (Fig. 3a) are fairly polydispersed with respect to the size distribution. The average diameter and coefficient of variation (CV) estimated using ImageJ software are 2.56 μm and 11.66%, respectively. The surface of the BC core appears smooth with clear boundaries and is almost free from aggregation. The surface of the BC core became heterogeneous after the formation of the BC@CCp composite (Fig. 3b) *via* the seeded chemical

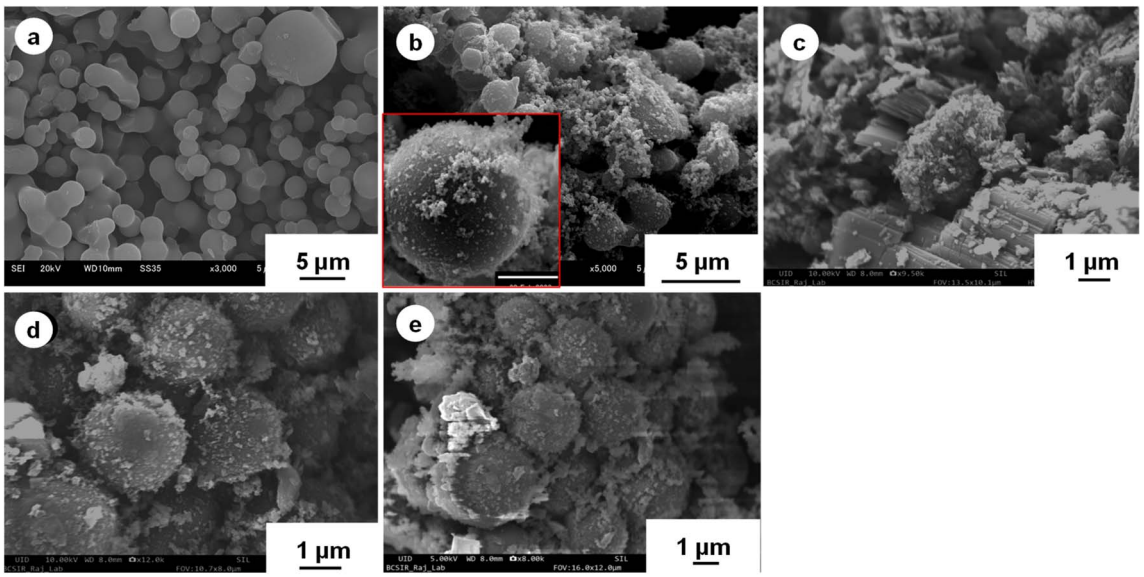

Fig. 3 SEM images of the BC core (a), BC@CCp composite (b), calcined V_2O_5 (c) and BC@CCp@V_2O_5 hybrid composite (d and e) particles.

oxidative copolymerization of aniline with pyrrole. The tiny particles attached to the surface are perhaps the electroactive (Ani–Py) copolymer, *i.e.*, CCp. It is apparent from the image that due to the limited surface area, some independent copolymer particles are formed. In some instances, the tiny independent particles are perhaps organized into hairy structures on the BC surface. For clear identification, an inset image of one comparatively larger BC@CCp composite particle is shown in Fig. 3b. The mean diameter and CV of BC@CCp composite particles are 2.90 μm and 9.6%, respectively. The calcined V_2O_5 particles shown in Fig. 3c have different shaped morphologies, *e.g.*, corpuscular (spherical and ellipsoid), linear (rod), flake and sheet types. The size distribution of V_2O_5 particles is broad, and the smaller particles have dimensions less than 100 nm. The surface morphology of the BC@CCp@V_2O_5 hybrid composite (Fig. 3d and e) is considerably different from that of the reference BC@CCp composite particles. The surface heterogeneity increases, and tiny particles similar to V_2O_5 can be seen adhered to the surface of the hybrid composite. The increase in the density of adhered tiny particles on the surface of the BC@CCp composite is another indication of hybrid composite formation with V_2O_5. Under the preparation conditions, there should be some free V_2O_5 particles, but their presence could not be confirmed from the image (Fig. 3d and e). The mean diameter of BC@CCp@V_2O_5 hybrid particles increases to 3.86 μm. Overall, results confirm the formation of conductive hybrid composite particles with V_2O_5 attached to the surface *via* some solid-phase interactions created *via* rubbing, polymer layer deformation, entanglement within the hairy network, and solid bridge formation, which can take place even at room temperature.[52,53]

The morphologies of BC@CCp, calcined V_2O_5 and BC@CCp@V_2O_5 were further analyzed by TEM observation. The TEM image of BC@CCp composite particles (Fig. 4a) confirms the hairy growth of CCp on the surface of BC particles. As such, the surface of composite particles becomes non-smooth and heterogeneous after seeded oxidative copolymerization. An identical observation is also made in the SEM image of BC@CCp composite particles (Fig. 3b). Comparatively, the surface of the BC@CCp@V_2O_5 hybrid composite particle (Fig. 4c) is slightly different, containing a network of smaller particles. In the network, around the dark-colored spherical BC particles, we can see various-shaped V_2O_5 particles, including a rod-shaped particle, as indicated by an arrow in Fig. 4c.

XPS, a surface-sensitive analytical tool, was used to understand the basic elemental constituents and valence states of vanadium in V_2O_5. In addition to the carbon and oxygen signals, the XPS survey spectrum of the BC@CCp composite (Fig. 5a) shows the presence of N1s, which is derived from the CCp layer. Furthermore, the spectrum of the BC@CCp@V_2O_5 hybrid composite (Fig. 5c) shows the existence of the $V2p^3$ signal at ~525 eV. The signal intensity of $V2p^3$ in the BC@CCp@V_2O_5 hybrid composite is obviously lower than that in native V_2O_5. The atom percentages of carbon, oxygen and nitrogen elements in the BC@CCp@V_2O_5 hybrid composite are not worth mentioning because it is prepared by simple mechanical blending.

The valence states of vanadium were further evaluated in the calcined V_2O_5 and BC@CCp@V_2O_5 hybrid composite *via* the deconvolution of the core-line spectrum of vanadium. As can be seen in Fig. 6a, the core-line signal of $V2p^3$ in calcined V_2O_5 can be differentiated into two signals corresponding to $V2p_{3/2}$ and $V2p_{1/2}$ at 516.6 eV and 524.0 eV, respectively. The separation of the spin–orbit component by 7.4 eV confirms V^{5+} as the dominant fraction.[38,54] The deconvoluted $V2p_{3/2}$ core-level spectrum exhibits two peaks at 515.4 and 516.6 eV, representing the oxidation states of vanadium (V^{4+} and V^{5+}), respectively.[55] V^{5+} accounts for 66.9% of the peak area, while V^{4+} constitutes only 2.8%. The other peak at 518.1 eV is assignable to the X-ray satellite of the O1s core-level.[55] Similar findings are observed from the deconvolution of the $V2p^3$ core-line signal for the BC@CCp@V_2O_5 hybrid composite (Fig. 6b). However, the

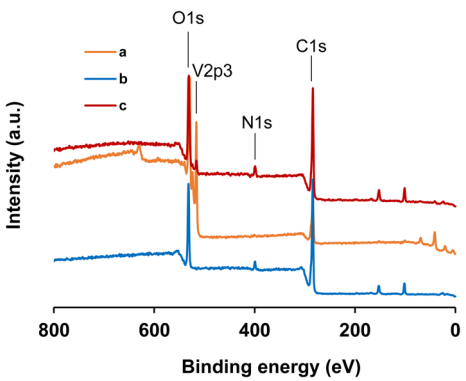

Fig. 5 XPS survey spectra of the BC@CCp composite (a), calcined V_2O_5 (b) and BC@CCp@V_2O_5 hybrid composite (c) particles.

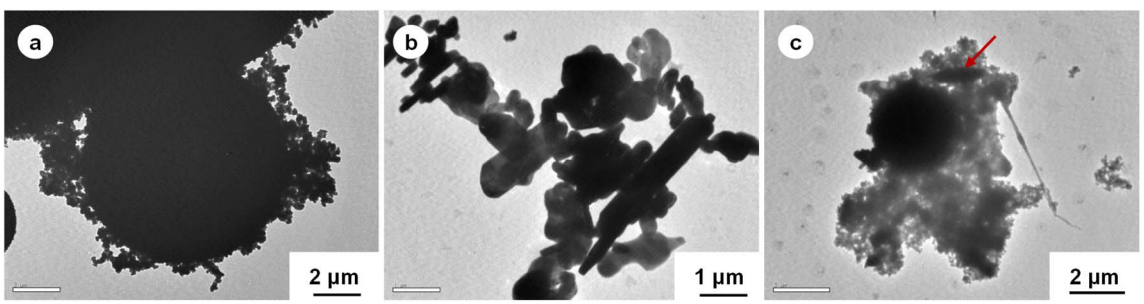

Fig. 4 TEM images of the BC@CCp composite (a), calcined V_2O_5 (b) and BC@CCp@V_2O_5 hybrid composite (c) particles.

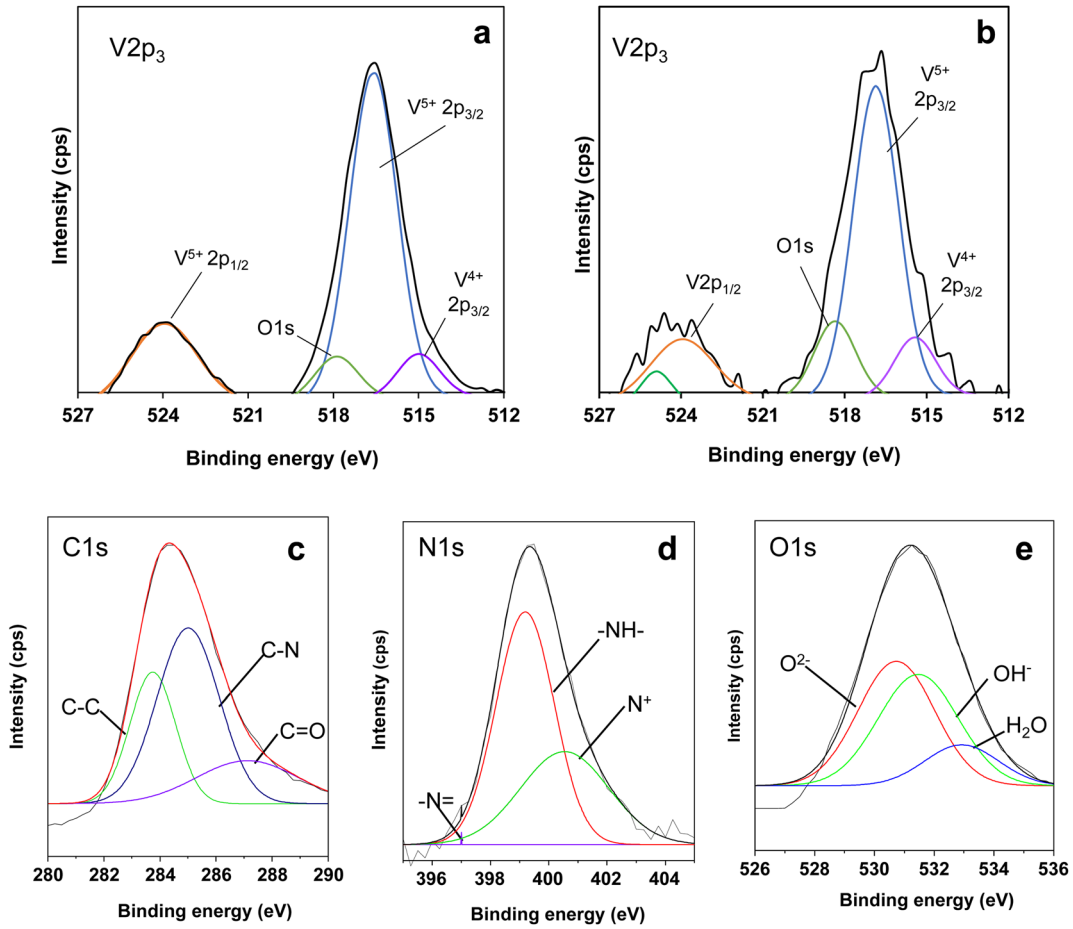

Fig. 6 XPS deconvoluted core-line spectra of V2p[3] (a and b), C1s (c), N1s (d) and O1s (e) in the calcined V_2O_5 (a) and BC@CCp@V_2O_5 hybrid composite (b–e) particles.

binding energies for V^{4+} and V^{5+} oxidation states and O1s are slightly shifted to 516.4, 516.9, and 518.3 eV in the hybrid composite, respectively. The enrichment of the higher-valence V^{5+} state to 72.4% in the hybrid composite may account for this positive deviation in the binding energy.[56] The positive deviation in the binding energy may also occur from a variation in the chemical environment.[56] In the present case, the change in the chemical environment around the vanadium nucleus due to the presence of an electron-rich CCp chain is less likely because the hybrid composite is prepared by the simple mechanical blending of two solid powders.[56] However, it is not yet known whether the solid-phase interaction during mechanical blending produces a positive shift in the binding energy.

The C1s core-line spectrum of the ultimate BC@CCp@V_2O_5 hybrid composite (Fig. 6c) can be deconvoluted into three bonding groups attributed to C–C, C–N and carbonyl/quinone at approximately 284.2, 285.5 and 287.9 eV, respectively.[12] The deconvolution of the N1s core-line spectrum (Fig. 6d) results in three signals at approximately 398.6, 400.0 and 401.2 eV, corresponding to –N= (imine), –NH– (amine) and N^+ (oxidized amine) groups, respectively. Furthermore, the O1s core-line peak (Fig. 6e) can be deconvoluted into three peaks at approximately 530.7, 531.5, and 533.0 eV. The peaks at 530.7 and 531.5 eV are assigned to V–O and V–OH bonds, respectively.[57] The other peak at 533.0 eV is related to the adsorbed H_2O–OH, where –OH groups are hydrogen-bonded to H_2O. Regardless of the interactions, all these structural and chemical component analyses confirm the incorporation of V_2O_5 in the hybrid composite.

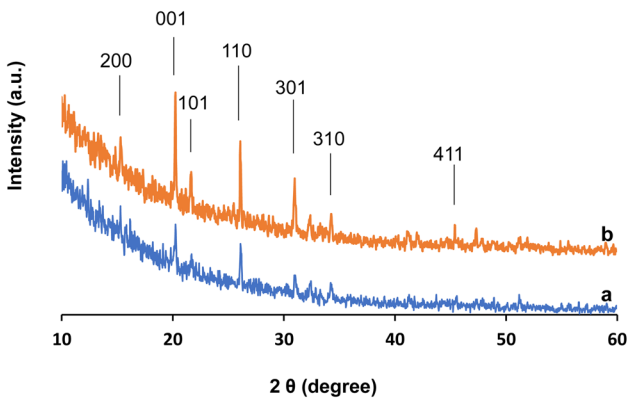

Fig. 7 XRD patterns of calcined V_2O_5 (a) and BC@CCp@V_2O_5 hybrid composite (b) particles.

The XRD pattern of calcined V_2O_5 (Fig. 7a) shows the characteristic peaks of the orthorhombic crystal structure of V_2O_5 at 2θ values of 15.28°, 20.22°, 21.66°, 26.11°, 30.99°, 34.21° and 45.52°, corresponding to the (200), (001), (101), (110), (301), (310) and (411) lattice planes (JCPDS 41-1426), respectively.[58] These characteristic peaks are also present in the BC@CCp@V_2O_5 hybrid composite, sometimes with slight deviations. In calcined V_2O_5, the (001) lattice plane at 20.22° has the highest intensity, with a *d*-spacing of 4.388 Å, while in the hybrid composite, the same peak has an almost identical *d*-spacing of 4.386°. However, the peak intensity of the respective (001) and (110) lattice planes considerably increases in the hybrid composite. The shift of the (110) lattice plane at 26.11° in calcined V_2O_5 to a lower angle of 26.05° in the hybrid composite indicates the expansion of the interlayer distance.[59] This enlarged interlayer distance will favorably enhance the accessible contact area for the electrolyte and hence the electrochemical performance of the cell.[60] The mean crystallite sizes of V_2O_5 in the calcined V_2O_5 and BC@CCp@V_2O_5 hybrid composite, estimated from the Debye–Scherrer equation using the diffraction signal, are 48.2 and 40.1 nm, respectively. The decrease in the crystallite size in the hybrid composite is possibly induced by the blending operation and solid-phase interaction.

3.2. Electrochemical performance

CV measurements were carried out for BC@CCp-, calcined V_2O_5- and BC@CCp@V_2O_5-coated graphite electrodes in a 1.0 M KCl solution at 25 °C. Independent of the electrode nature, rectangular-shaped CV curves (Fig. 8(A)a) are obtained in the −0.2 V to +0.6 V potential range at a fixed scan rate (50 mV s^{-1}). It is also apparent that the doping–dedoping reaction progresses almost reversibly. This behavior suggests that the fabricated graphite electrodes possess good capacitive performance. Moreover, the BC@CCp@V_2O_5-coated graphite electrode demonstrates better current response than the two other coated graphite electrodes (Fig. 8(A)b and c). Alternatively, it can be seen from Fig. 8(A)a that the CV curve of the BC@CCp@V_2O_5-coated graphite electrode has the highest integral area and hence the highest capacitance value among all three fabricated electrodes.[61] Obviously, the incorporation of CCp, calcined V_2O_5 and BC in the hybrid composite increases the number of electro-conductive sites and thus contributes to the faradaic redox process more aggressively at the electrode–electrolyte junction.

To obtain information about the rate capability, the electrochemical performance of the best-performing BC@CCp@V_2O_5 hybrid composite-coated electrode was further tested by recording CV curves at different scan rates ranging from 10 to 100 mV s^{-1}. The findings shown in Fig. 8B display that the peak current improves with an increase in the scan rate while almost preserving the shape of CV curves. The retention of the reversible charging–discharging process and favorable rate capability over a broad range of scan rates prove the potential of the fabricated BC@CCp@V_2O_5 electrode as an electroactive material.[62] To explore the optimal potential window, the CV curves were also recorded in different potential windows from −0.2 V to +1.0 V at a constant scan rate of 50 mV

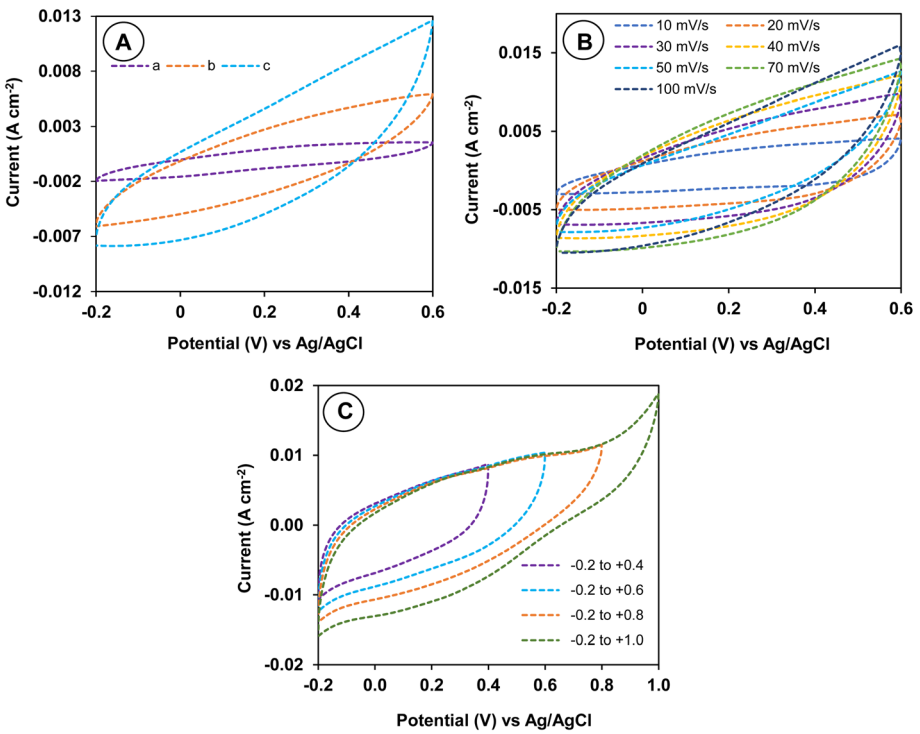

Fig. 8 (A) CV curves of the BC@CCp composite- (a), calcined V_2O_5- (b) and BC@CCp@V_2O_5 hybrid composite-coated (c) graphite electrodes at a scan rate of 50 mV s^{-1}. (B and C) CV curves of the BC@CCp@V_2O_5 hybrid composite-coated graphite electrode at different (B) scan rates and (C) potential ranges.

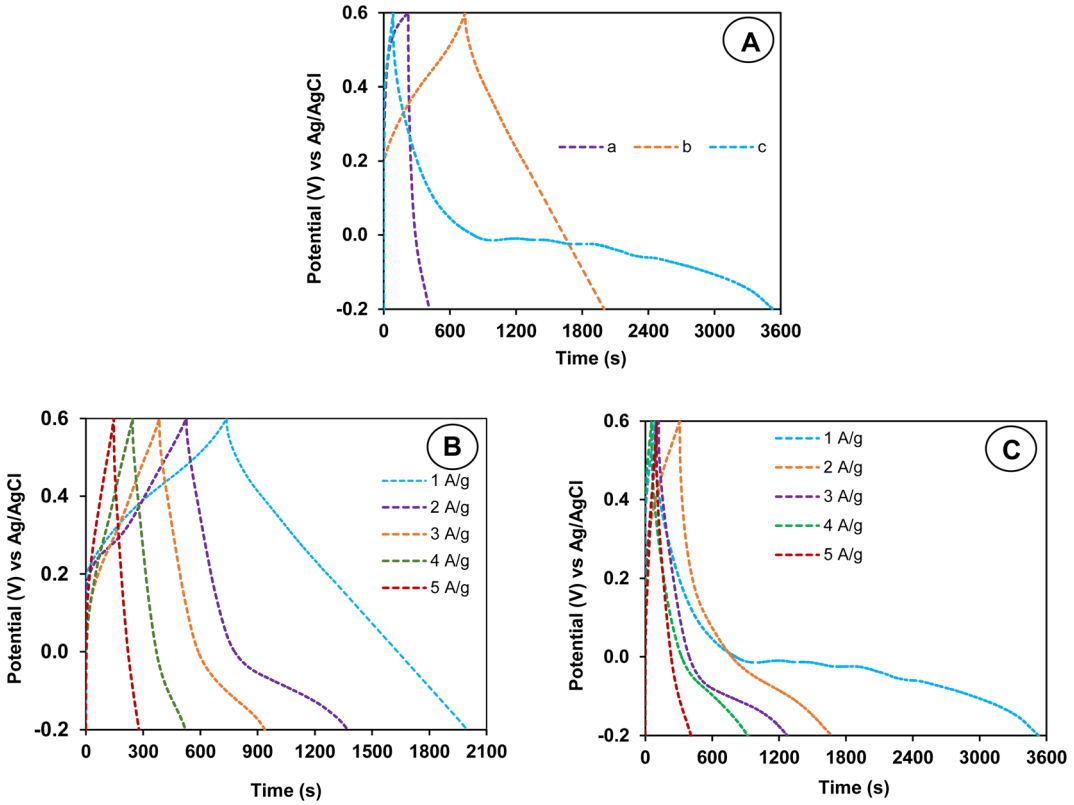

Fig. 9 (A) GCD curves of BC@CCp- (a), calcined V_2O_5- (b) and BC@CCp@V_2O_5-coated (c) graphite electrodes at a constant current density of 1.0 A g^{-1}. (B and C) GCD curves of calcined V_2O_5- (B) and BC@CCp@V_2O_5-coated (C) graphite electrodes at different current densities.

s^{-1}. The almost-rectangular-shaped CV curves (Fig. 8C) demonstrate that the electrode coated with the hybrid composite possesses good capacitive behavior in the potential range up to 1.0 V. Therefore, the overall comparative analysis of CV results indicates that the improved compatibility among carbon-rich BC, conducting copolymer and V_2O_5 considerably enhances the electrochemical performance and rate capability.

After CV experiments, the same modified graphite electrodes were utilized for GCD measurements (Fig. 9(A)a) in the identical potential region from −0.2 V to +0.6 V, and the current density was fixed at 1.0 A g^{-1}. This shows that the fabricated graphite electrode is stable because the color of the electrolyte does not noticeably change owing to the diffusion or solubilization of coated conducting materials. All GCD curves show an insignificant IR drop. This finding is an indication of good capacitive behavior in reversible electrochemical processes.[63] Interestingly, the BC@CCp@V_2O_5 composite-coated graphite electrode has a longer discharge time compared to its charging time after the inclusion of three components, *i.e.*, BC, CCp and V_2O_5 in the same electrode. This charging–discharging behavior is desirable for high-performance energy storage materials.[63] Comparatively, such behavior is not observed for the two other fabricated graphite electrodes (Fig. 9(A)b and c). The specific capacitances obtained from the respective GCD curves of BC@CCp-, calcined V_2O_5- and BC@CCp@V_2O_5-coated electrodes are 243.2, 2498.2 and 4150.6 F g^{-1}, respectively. The enhancement and superiority of the capacitance value of the BC@CCp@V_2O_5-coated electrode indicate the comparable synergistic interaction and compatibility among the carbon-rich BC, electroconductive copolymer, calcined V_2O_5 and graphite rod.[64,65] Relatively, the higher energy storage efficiency of the BC@CCp@V_2O_5-coated graphite electrode is thus facilitated by good contact among different electroactive phases and the better transport of electrons or ions through conducting channels. After the GCD experiment, the influence of different current densities (1.0 to 5.0 A g^{-1}) on the GCD potential was examined for calcined V_2O_5- (Fig. 9B) and BC@CCp@V_2O_5-coated graphite electrodes (Fig. 9C). The retention of charge–discharge behavior independent of the current density implies good rate capability. Fig. 9B and C also indicates that a decrease in the current density prolongs the charge–discharge time. The

Table 1 Specific capacitance calculated from GCD curves at different current densities

Current density (A g^{-1})	Specific capacitance (F g^{-1})		
	BC@CCp	Calcined V_2O_5	BC@CCp@V_2O_5
1	243.25	2498.2	4150.6
2	291.25	2147.2	2936.5
3	314.625	2038.1	2628.4
4	218.5	1389.5	1903.5
5	135.25	840.6	1814.4

values of the specific capacitance of different fabricated electrodes calculated from GCD plots are shown in Table 1. The gradual decrease in the specific capacitance at higher current densities apparently originates from slower charge diffusion, limited faradaic reactions and impassable electrochemically active surface areas.[62] The slower charging–discharging kinetics at higher current densities thus decreases the electrode efficiency.[66] Despite the decrease in the specific capacitance with increasing current density, the BC@CCp@V_2O_5-coated electrode still displays high capacitance, which decreases from 4150.6 F g^{-1} at 1.0 A g^{-1} to 1814.4 F g^{-1} at 5.0 A g^{-1}. It is apparent from Table 1 that the BC@CCp@V_2O_5-coated graphite electrode retains ~44.0% of the original capacitance value at a higher current density of 5 A g^{-1}, which confirms the substantial sustainability and rate capability. Previously, we observed that high current density does not have a significant influence on the specific capacitance for the BC@CCp-coated electrode. It was predicted that BC, containing active binding sites (*e.g.*, –OH/ester/ether/carboxyl), and electroactive nitrogen-rich CCp comprising P(Ani–Py) would produce a stable and compact network that would partially inhibit the volume change during charging–discharging operation.[12] This same phenomenon also plays a role in the improved sustainability and excellent rate performance of the BC@CCp@V_2O_5-coated graphite electrode. Therefore, in agreement with CV results, GCD measurements also show a remarkable improvement in the specific capacitance, sustainability and rate performance after the integration of V_2O_5 into BC@CCp. However, more efforts can be made to enhance sustainability at higher current densities *via* the *in situ* nucleation and growth of V_2O_5 nanoparticles in the presence of BC@CCp because such methods should produce a more stable compact network.

When BC, CCp, and V_2O_5 are combined into a single hybrid composite, the electrochemical performance is boosted. BC provides a conductive backbone that supports the movement of electrons across the composite. The conductive copolymer, CCp, acts as an additional electron transfer medium, enhancing the electron conductivity *via* its redox property. V_2O_5 adds a high-capacitance mechanism *via* its ability to undergo redox reactions, further boosting the electrochemical performance. During the charging process, ions from the electrolyte intercalate into the nanocomposite structure, and V_2O_5 and CCp undergo redox reactions. BC assists the electron flow between CCp and V_2O_5, maximizing charge storage. V_2O_5 exhibits pseudocapacitance *via* faradaic reactions, where V_2O_5 undergoes a reversible change in oxidation states during charge–discharge cycles. During charging, V_2O_5 undergoes reduction because it accepts an electron (*e.g.*, from V^{5+} to V^{4+}), and during discharge, V_2O_5 is oxidized (*e.g.*, from V^{4+} to V^{5+}). BC and CCp, *via* solid-phase interactions, help prevent the loss and agglomeration of V_2O_5 particles, keeping them distributed and accessible for redox reactions. This leads to the better mechanical stability and improved charge–discharge performance of the supercapacitor.

To obtain the surface electrochemical information, the PEIS of the respective fabricated graphite electrode was investigated, and the related Nyquist plots are shown in Fig. 10A. The Nyquist plot generally has two segments: one is a higher-frequency semicircle zone and the other is a straight-line region at lower frequencies. Here, the absence of the semicircle segment at higher frequencies indicates that neither of the fabricated electrodes hinders the electron flow from the electrolyte to the inner part of the electrode.[67] Additionally, the maximum slope of the low-frequency straight-line region in the plot of the BC@CCp@V_2O_5-coated graphite electrode (Fig. 10(A)c) suggests that the electrode possesses excellent capacitance performance with the least diffusion resistance.[44,68,69] The equivalent circuit of the BC@CCp@V_2O_5 hybrid composite-coated electrode is shown in Fig. 10B, where R_1 is the resistance of the coating layer, R_2 is the resistance to charge transfer, and Warburg impedance W_o corresponds to the faradaic impedance. The parallel connection between the constant phase element (CPE) and R_2 is referred to as the charge-transfer-limiting process.

The long-time cycling performance of BC@CCp-, calcined V_2O_5- and BC@CCp@V_2O_5-coated graphite electrodes was evaluated *via* GCD cycle experiments. The experiment was

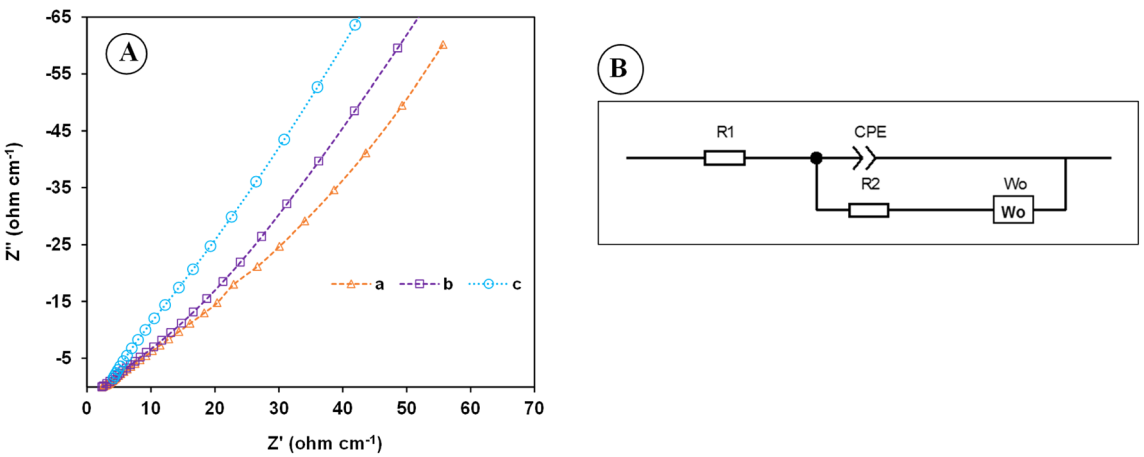

Fig. 10 (A) The Nyquist plots of the PEIS of BC@CCp- (a), calcined V_2O_5- (b) and BC@CCp@V_2O_5-coated (c) graphite electrodes in a 1.0 M KCl solution over in frequency range from 5×10^{-2} to 5×10^{-5} Hz measured at a 50 mV s^{-1} scan rate. (B) A sample equivalent circuit fitted with the Nyquist plot.

performed up to 1000 cycles at a current density of 10.0 A g^{-1}, and the potential range was identical from −0.2 V to +0.6 V. During the experiment, no visible change in the electrolyte color due to the peeling off of electroactive materials from the graphite electrode was observed. As illustrated in Fig. 11A, the reference BC@CCp- and calcined V_2O_5-coated electrodes demonstrate a slightly downward trend in capacitance values, expressed as retention stability in percentage, which decreases to 96.6% and 83.3%, respectively, after 1000 cycles. The incorporation of BC and formation of a stable network *via* hydrogen bonding between the BC functional groups and electroactive copolymer reduces the extent of degradation during repeated charging–discharging operations. BC@CCp mostly follows a combination of type I and type II cycle stabilities, and the charge storage is accompanied by reversible processes of the adsorption–desorption of ions and electrochemical redox reactions at the electrode–electrolyte junction.[70] Importantly, when calcined V_2O_5 is only mechanically blended with BC@CCp, the capacitance of the resultant BC@CCp@V_2O_5-coated graphite electrode first slightly decreases, then gradually increases to 134% up to 800 cycles, and finally remains almost steady. The initial decrease in the specific capacitance up to the 26th cycles is perhaps due to the insufficient wetting of the BC@CCp@V_2O_5-coated electrode surface by the aqueous KCl electrolyte

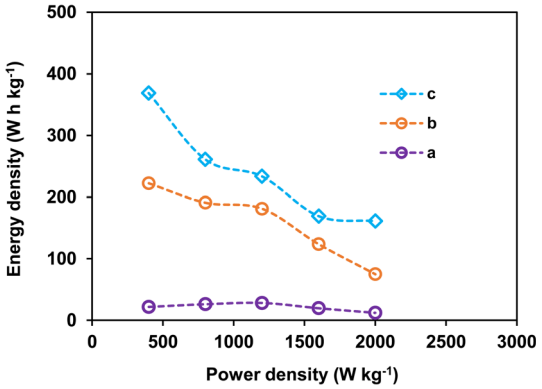

Fig. 12 Ragone plot of the BC@CCp@V_2O_5 hybrid composite-coated graphite electrode studied at current densities of 1.0–5.0 A g^{-1}.

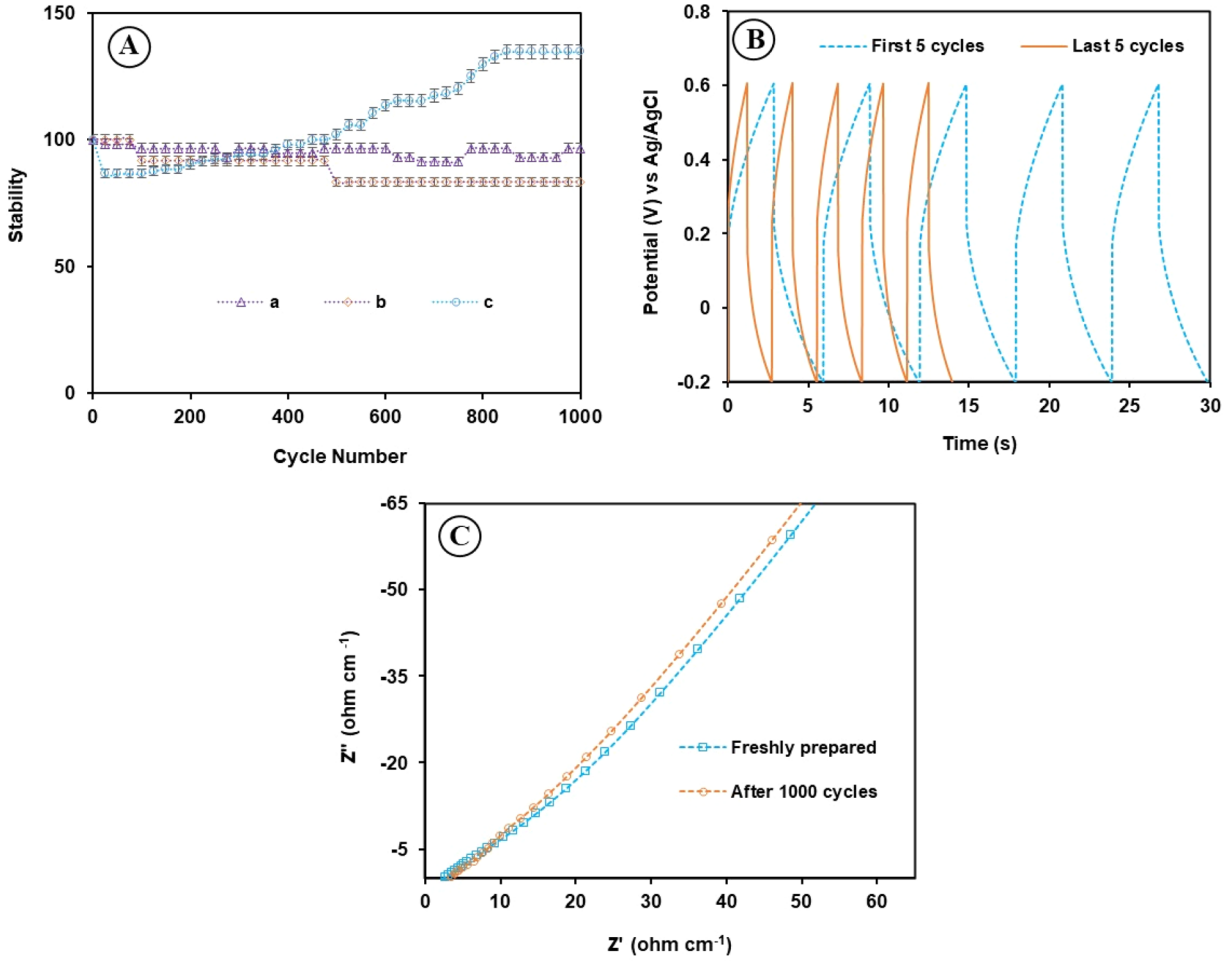

Fig. 11 (A) Cycling stability of the BC@CCp- (a), calcined V_2O_5- (b) and BC@CCp@V_2O_5-coated (c) graphite electrodes estimated from GCD curves in a 1.0 M KCl solution at a current density of 10.0 A g^{-1}. (B) Charging–discharging behavior of the BC@CCp@V_2O_5-coated graphite electrode *versus* time during the first and last five cycles. (C) Nyquist plots recorded for the fresh BC@CCp@V_2O_5-coated graphite electrode and the same electrode after 1000 charge–discharge cycles.

Table 2 Electrochemical properties of V_2O_5-based nanocomposite supercapacitors

Composite	Electrolyte	Current density ($A\ g^{-1}$)	Capacitance ($F\ g^{-1}$)	Power density ($W\ Kg^{-1}$)	Energy density ($Wh\ Kg^{-1}$)	Ref.
C@V_2O_5 nanorods	0.5 M K_2SO_4	0.5	417	170	9.4	29
V_2O_{5-x}@C composite	1 M KCl	1	277.6 mA h g^{-1}	—	—	30
RGO/V_2O_5	—	1	320	—	—	31
Graphene/V_2O_5	—	1	189	—	—	32
V_2O_5/CNTs-SAC	2 M $NaNO_3$	10	357.5	—	—	33
V_2O_5/f-MWCNT	—	0.5	410	121	8.9	35
V_2O_5@PPy	—	0.2	344	—	—	38
PEDOT-VO	—	0.5	370.5 mA h g^{-1}	—	—	40
Vo-V_2O_5/CP	1 M Na_2SO_4	0.5	614	—	—	41
PANI/GO-V-APS	1 M H_2SO_4	0.5	712	—	—	42
V_2O_5/MWCNTs	$LiClO_4$	1.0	160.15	2300	27.07	73
V_2O_5-pBOA-graphene	—	1.0	986		49	74
rGO/V_2O_5	Organic electrolyte	0.1	384	275	80.4	75
Graphene/VO_x	—	1.0	1110	72	54	76
V_2O_5/rGO	KCl	1.0	635	900	79.5	77
V_2O_5-PAni	LiCl	0.5 ($mA\ cm^{-2}$)	443	720	69.2	78
V_2O_5-PAni	$LiClO_4$	1.0 ($mA\ cm^{-2}$)	1115	—	—	79
V_2O_5/rGO	Aqueous	1.0	537	500	74.58	80
V_2O_5@PPy		1.0	307	161	37	65
BC@CCp@V_2O_5	KCl	1.0	4150.6	400	368.9	This work

solution at the threshold of the electrochemical process because this is a compact hybrid structure of three components.[71,72] Subsequently, the gradual increase in the specific capacitance may have come from the wetting and electro-activation of the electrode surface by the electrolyte solution during the cycling experiment. It is also probable that under the applied electric field, more V^{5+} becomes available at the electrode surface for redox reactions. Furthermore, stable composite formation *via* solid-phase interactions between the BC@CCp and calcined V_2O_5 powder inhibits the structural collapse of V_2O_5, which occurred in the case of the V_2O_5-coated electrode. As a direct proof, the GCD curves of the first five cycles are compared with the last five cycles in Fig. 11B. This figure shows that the charge–discharge time is lower in the first five cycles than in the last five cycles. The enhancement in the cycle stability of the BC@CCp@V_2O_5-coated graphite electrode is further confirmed using PEIS study and the corresponding Nyquist plots of the as-coated graphite electrode before and after 1000 charge–discharge cycles, as shown in Fig. 11C. The slight increase in the slope of the low-frequency straight-line region from the electrode after 1000 cycles indicates an increase in the capacitive performance and a decrease in the diffusion resistance. The porous and interconnected network of BC enables better mechanical interlocking and stress distribution and minimizes cracking or detachment of the active material during electrochemical operation. This synergistic effect ensures long-term cycling stability while maintaining low interfacial resistance.

In order to justify the application potential of the fabricated graphite electrodes in energy storage devices, comparative Ragone plots, showing the relationship between the energy density and power density, are given in Fig. 12. The fabricated graphite electrode made from the BC@CCp@V_2O_5 hybrid composite possesses the highest energy density of 368.9 Wh kg^{-1} when the power density is 400 W kg^{-1}. Results suggest that the prepared hybrid composite possesses very high capacity, reasonably good for efficient use in supercapacitor electrodes.

To understand the application viability, the specific capacitance, energy, and power density values of the BC@CCp@V_2O_5 hybrid composite-coated graphite electrode are compared with literature values of some V_2O_5-based composite electrode materials (Table 2). It is evident that our fabricated hybrid composite-coated graphite electrode is better, at least in terms of the specific capacitance and energy density.

The findings suggest that the integration of three components (*i.e.*, carbon-rich BC, conducting copolymer and V_2O_5) into a hybrid composite and subsequent coating on a graphite electrode produces a stable network *via* hydrogen bonding and solid-phase interactions. Such a strong and stable network remarkably improves the capacitance value, capacitance retention, cycle stability, and rate capability, which have rarely been observed for other hybrid electrode materials, as stated in the literature.

4. Conclusions

In this study, BC, a carbon-rich biomass, is utilized for hosting a conducting copolymer and a metal oxide, *i.e.*, CCp and calcined V_2O_5. The objective is to determine the utility of BC as a low-cost, easily accessible green material for developing sustainable electrode materials for supercapacitor applications. First, the 2.56 μm sphere-shaped BC core particles are prepared by the simple hydrothermal treatment of a 0.8 M sucrose solution at 180 °C. Then, BC@CCp composite particles are synthesized by the *in situ* chemical oxidative copolymerization of aniline and pyrrole while maintaining the w/w ratio of BC to CCp at 1 : 1. Finally, the ultimate BC@CCp@V_2O_5 hybrid

composite is produced by mechanically blending a mixture of BC@CCp and calcined V_2O_5 in a w/w ratio of 4 : 1. The size distribution and surface morphology analyses indicated the formation of the hybrid composite *via* the solid-phase synergy between the BC@CCp composite and V_2O_5. XPS analysis revealed the domination of vanadium in the V^{5+} oxidation state. The electrochemical performance of BC@CCp-, calcined V_2O_5- and BC@CCp@V_2O_5-coated graphite electrodes is measured and compared using CV, GCD, and PEIS curves. The specific capacitances of BC@CCp-, calcined V_2O_5-, and BC@CCp@V_2O_5-coated electrodes are 243.2, 2498.2, and 4150.6 F g^{-1} at a current density of 1.0 A g^{-1}, respectively. In addition to the maximum specific capacitance, the BC@CCp@V_2O_5-coated graphite electrode displays an enhanced rate capacity, low charge transfer resistance, and good cycle stability. Importantly, the BC@CCp@V_2O_5-coated electrode exhibits quick charging and relatively long discharging times during GCD cycle experiments. The fabricated electrode also shows a high energy density of 368.9 Wh kg^{-1} at a power density of 400.0 W kg^{-1}. Thus, the V_2O_5-integrated BC@CCp hybrid composite has good potential for use as a sustainable electrode material, and BC is a good platform for hosting CCp and V_2O_5 for designing highly efficient supercapacitor electrodes. There is also a good prospect of further enhancing the electrochemical performance by reducing the size distribution of anchored V_2O_5 to the nanorange.

Data availability

The data supporting this article have been included as part of the manuscript.

Author contributions

Md. Mahabur Rahman: methodology, investigation, formal analysis, data curation, validation, and writing – original draft. Abdulla Al Mamun: methodology, investigation, formal analysis, and data curation, validation. Hideto Minami: investigation and data curation. Md. Kawsar Hossain: investigation and data curation. S. Manjura Hoque: investigation and data curation. Mostafa K. Sharafat: resources. Hasan Ahmad: supervision, conceptualization, data curation, resources, project administration, and writing – review and editing.

Conflicts of interest

The authors have no competing interests to declare that are relevant to the content of this article.

Acknowledgements

The author (HA) acknowledges the instrument support from the Central Science Laboratory, Rajshahi University. The author (HA) acknowledges the research grant under special allocation (FY 2024-2025) from UGC, Dhaka.

References

1 J. Yuan, Y. Li, G. Lu, Z. Gao, F. Wei, J. Qi, Y. Sui, Q. Yan and S. Wang, Controlled synthesis of flower-like hierarchical NiCo-layered double hydroxide integrated with metal-organic framework-derived Co@C for supercapacitors, *ACS Appl. Mater. Interfaces*, 2023, **15**(30), 36143–36153, DOI: **10.1021/acsami.3c05061**.

2 J. Zhao and A. F. Burke, Electrochemical capacitors: Materials, technologies and performance, *Energy Storage Mater.*, 2021, **36**, 31–55, DOI: **10.1016/j.ensm.2020.12.013**.

3 A. Zaka, K. Hayat and V. Mittal, Recent trends in the use of three-dimensional graphene structures for supercapacitors, *ACS Appl. Electron. Mater.*, 2021, **3**(2), 574–596, DOI: **10.1021/acsaelm.0c00953**.

4 S. Liu, L. Wei and H. Wang, Review on reliability of supercapacitors in energy storage applications, *Appl. Energy*, 2020, **278**, 115436, DOI: **10.1016/j.apenergy.2020.115436**.

5 J. Libich, J. Máca, J. Vondrák, O. Čech and M. Sedlaříková, Supercapacitors: properties and applications, *J. Energy Storage*, 2018, **17**, 224–227, DOI: **10.1016/j.est.2018.03.012**.

6 T.-B. Nguyen, K. Sherpa, X.-T. Bui, V.-T. Nguyen, T.-D.-H. Vo, H.-T.-T. Ho, C.-W. Chen and C.-D. Dong, Biochar for soil remediation: A comprehensive review of current research on pollutant removal, *Environ. Pollut.*, 2023, **337**, 122571, DOI: **10.1016/j.envpol.2023.122571**.

7 L. Lv, S. Huang and H. Zhou, Effect of introducing chemically activated biochar as support material on thermal properties of different organic phase change materials, *Solar Energy Mater. Solar Cells*, 2024, **264**, 112617, DOI: **10.1016/j.solmat.2023.112617**.

8 E. D. Visser, N. S. Ntalane and L. Khotseng, Catalytic properties of biochar as support material potential for direct methanol fuel cell: A review, *ACS Omega*, 2023, **8**(44), 40972–40981, DOI: **10.1021/acsomega.3c02283**.

9 Y. L. Yaphary, M. He, G. Lu, F. Zou, P. Liu, D. C. W. Tsang and Z. Leng, Experiment and multiscale molecular simulations on the Cu absorption by biochar-modified asphalt: An insight into removal capability and mechanism of heavy metals from stormwater runoff, *Chem. Eng. J.*, 2023, **462**, 142205, DOI: **10.1016/j.cej.2023.142205**.

10 M. He, Z. Xu, D. Hou, B. Gao, X. Cao, Y. S. Ok, J. Rinklebe, N. S. Bolan and D. C. W. Tsang, Waste-derived biochar for water pollution control and sustainable development, *Nature Rev. Earth Environ.*, 2022, **3**(7), 444–460, DOI: **10.1038/s43017-022-00306-8**.

11 Y. Lin, F. Li, X. Li, H. Zhao and G. Liu, Multifunctional template prepares N-, O-, and S-codoped mesoporous 3D hollow nanocage biochar with a multilayer wall structure for aqueous high-performance supercapacitors, *ACS Appl. Energy Mater.*, 2023, **6**(4), 2265–2275, DOI: **10.1021/acsaem.2c03427**.

12 M. M. Rahman, A. A. Mamun, H. Minami, M. M. Rahman, S. M. Hoque and H. Ahmad, Biochar/poly(aniline-pyrrole) modified graphite electrode and electrochemical behavior

for application in low-cost supercapacitor, *Arabian J. Chem.*, 2024, **17**(9), 105938, DOI: 10.1016/j.arabjc.2024.105938.

13 G. Tan and H. Q. Yu, Rethinking biochar: black gold or not?, *Rev. Mater.*, 2024, **9**(1), 4–5, DOI: 10.1038/s41578-023-00634-1.

14 M. S. Ali, M. M. Rahman, M. K. Hossain, H. Minami, M. M. Rahman, S. M. Hoque, M. A. Alam and H. Ahmad, Impact of mesoporous SiO_2 support for Ni/polypyrrole nanocomposite particles on their capacitive performance, *New J. Chem.*, 2022, **46**(45), 21798–21811, DOI: 10.1039/D2NJ04320C.

15 A. Moyseowicz, D. Minta and G. Gryglewicz, Conductive polymer/graphene-based composites for next generation energy storage and sensing applications, *ChemElectroChem*, 2023, **10**(9), e20220115, DOI: 10.1002/celc.202201145.

16 M. Rashid, M. M. Islam, H. Minami, M. Aftabuzzaman, M. A. Rahman, M. M. Hossain, S. M. Hoque, M. A. Alam and H. Ahmad, Nickel decorated melamine-formaldehyde resin/polyaniline composites for high specific capacitance, *Mater. Chem. Phys.*, 2020, **249**, 122957, DOI: 10.1016/j.matchemphys.2020.122957.

17 J. Yang, Y. Liu, S. Liu, L. Li, C. Zhang and T. Liu, Conducting polymer composites: Material synthesis and applications in electrochemical capacitive energy storage, *Mater. Chem. Front.*, 2017, **1**(2), 251–268, DOI: 10.1039/C6QM00150E.

18 R. Megha, Y. T. Ravikiran, S. C. V. Kumari, T. Chandrasekhar and S. Thomas, Optimized polyaniline-transition metal oxide composites: A comparative study of alternating current conductivity via correlated barrier hopping model, *Polym. Compos.*, 2018, **39**(10), 3545–3555, DOI: 10.1002/pc.24375.

19 Z. Luo, Y. Zhu, E. Liu, T. Hu, Z. Li, T. Liu and L. Song, Synthesis of polyaniline/SnO_2 nanocomposite and its improved electrochemical performance, *Mater. Res. Bull.*, 2024, **60**, 105–110, DOI: 10.1016/j.materresbull.2014.08.022.

20 H. Ahmad, M. M. Rahman, M. A. Ali, H. Minami, K. Tauer, M. A. Gafur and M. M. Rahman, A simple route to synthesize conductive stimuli-responsive polypyrrole nanocomposite hydrogel particles with strong magnetic properties and their performance for removal of hexavalent chromium ions from aqueous solution, *J. Magnet. Magnet. Mater.*, 2016, **412**, 15–22, DOI: 10.1016/j.jmmm.2016.03.068.

21 H. Li, S. Yang, Y. Zhao, T. Tan, X. Wang and Z. Bakenov, Synthesis of ZnO/polypyrrole nanoring composite as high-performance anode materials for lithium-ion batteries, *J. Nanomater.*, 2019, **2019**, 4702849, DOI: 10.1155/2019/4702849.

22 X. Wang, T. Wang, D. Liu, J. Guo and P. Liu, Synthesis and electrochemical performance of CeO_2/PPy nanocomposites: Interfacial effect, *Indust. Eng. Chem. Res.*, 2016, **55**(4), 866–874, DOI: 10.1021/acs.iecr.5b03891.

23 A. Anand, N. Rani, P. Saxena, H. Bhandari and S. K. Dhawan, Development of polyaniline/zinc oxide nanocomposite impregnated fabric as an electrostatic charge dissipative material, *Polym. Int.*, 2015, **64**(9), 1096–1103, DOI: 10.1002/pi.4870.

24 J. Guo, Y. Sun, X. Li, S. Xi, M. M. Ibrahim, H. Qiu, G. A. M. Mersal, G. A. El-Bahy, V. Murugadoss, W. Abdul and F. Zhou, Hollow core-shell structure Fe_3O_4@polypyrrole composites for enhanced electromagnetic wave absorption, *Compos. Sci. Technol.*, 2024, **258**, 110917, DOI: 10.1016/j.compscitech.2024.110917.

25 S. Karthick, A. Sumisha and K. Haribabu, Performance of tungsten oxide/polypyrrole composite as cathode catalyst in single chamber microbial fuel cell, *J. Environ. Chem. Eng.*, 2020, **8**(6), 104520, DOI: 10.1016/j.jece.2020.104520.

26 A. De Adhikari, R. Oraon, S. K. Tiwari, J. H. Lee, N. H. Kim and G. C. Nayak, A V_2O_5 nanorod decorated graphene/polypyrrole hybrid electrode: a potential candidate for supercapacitors, *New J. Chem.*, 2017, **41**(4), 1704–1713, DOI: 10.1039/C6NJ03580A.

27 D. Chao, X. Xia, J. Liu, Z. Fan, C. F. Ng, J. Lin, H. Zhang, Z. X. Shen and H. J. Fan, A V_2O_5/conductive-polymer core/shell nanobelt array on three-dimensional graphite foam: a high-rate, ultrastable, and freestanding cathode for lithium-ion batteries, *Adv. Mater.*, 2014, **33**, 5794–5800, DOI: 10.1002/adma.201400719.

28 D. Chen, J. Li and Q. Wu, Review of V_2O_5-based nanomaterials as electrode for supercapacitor, *J. Nanopart. Res.*, 2019, **21**(9), 201, DOI: 10.1007/s11051-019-4645-8.

29 B. Saravanakumar, K. K. Purushothaman and G. Muralidharan, High performance supercapacitor based on carbon coated V_2O_5 nanorods, *J. Electroanal. Chem.*, 2015, **758**, 111–116, DOI: 10.1016/j.jelechem.2015.10.031.

30 C. Li, T. Liao, D. Chen, T. You, X. Jiang, M. Xu, H. Yu, G. Zhou, G. Li and Y. Chen, Fabrication of carbon-coated V_2O_{5-x} nanoparticles by plasma-enhanced chemical vapor deposition for high-performance aqueous zinc-ion battery composite cathodes, *Chinese Chem. Lett.*, 2024, **2024**, 110557, DOI: 10.1016/j.cclet.2024.110557.

31 H. Zhang, A. Xie, C. Wang, H. Wang, Y. Shen and X. Tian, Bifunctional reduced graphene oxide/V_2O_5 composite hydrogel: Fabrication, high performance as electromagnetic wave absorbent and supercapacitor, *ChemPhysChem*, 2014, **15**(2), 366–373, DOI: 10.1002/cphc.201300822.

32 S.-M. Lee, Y.-J. Park, J.-H. Kim and K. Lee, Effects of annealing on electrochemical performance in graphene/V_2O_5 supercapacitor, *Appl. Surf. Sci.*, 2020, **512**, 145626, DOI: 10.1016/j.apsusc.2020.145626.

33 M. Sathiya, A. S. Prakash, K. Ramesha, J.-M. Tarascon and A. K. Shukla, V_2O_5-anchored carbon nanotubes for enhanced electrochemical energy storage, *J. Am. Chem. Soc.*, 2011, **133**(40), 16291–16299, DOI: 10.1021/ja207285b.

34 Q. Wang, Y. Zou, C. Xiang, H. Chu, H. Zhang, F. Xu, L. Sun and C. Tang, High-performance supercapacitor based on V_2O_5/carbon nanotubes-super activated carbon ternary composite, *Ceramics Int.*, 2016, **42**(10), 12129–12135, DOI: 10.1016/j.ceramint.2016.04.145.

35 B. Saravanakumar, K. K. Purushothaman and G. Muralidharan, V_2O_5/functionalized MWCNT hybrid nanocomposite: The fabrication and its enhanced

supercapacitive performance, *RSC Adv.*, 2014, **4**(70), 37437–37445, DOI: 10.1039/C4RA05942E.

36 N. Vishwakarma, T. T. Mashangva, S. Rajput, T.-D. Pham, M. Kumar and A. Sharma, Unlocking the potential for revolutionary energy storage capabilities of V_2O_5/GO nanocomposites synthesized under microwave irradiation, *J. Energy Storage*, 2024, **103**, 114405, DOI: 10.1016/j.est.2024.114405.

37 L. Shao, J.-W. Jeon and J. L. Lutkenhaus, Polyaniline/vanadium pentoxide layer-by-layer electrodes for energy storage, *Chem. Mater.*, 2012, **24**(1), 181–189, DOI: 10.1021/cm202774n.

38 J.-G. Wang, H. Liu, H. Liu, W. Hua and M. Shao, Interfacial constructing flexible V_2O_5@ polypyrrole core-shell nanowire membrane with superior supercapacitive performance, *ACS Appl. Mater. Interfaces*, 2018, **10**(22), 18816–18823, DOI: 10.1021/acsami.8b05660.

39 Z. Tong, S. Liu, X. Li, Y. Ding, J. Zhao and Y. Li, Facile and controllable construction of vanadium pentoxide@conducting polymer core/shell nanostructures and their thickness-dependent synergistic energy storage properties, *Electrochim. Acta*, 2016, **222**, 194–202, DOI: 10.1016/j.electacta.2016.09.098.

40 S. Li, X. Wei, C. Wu, B. Zhang, S. Wu and Z. Lin, Constructing three-dimensional structured V_2O_5/conductive polymer composite with fast ion/electron transfer kinetics for aqueous zinc-ion battery, *ACS Appl. Energy Mater.*, 2021, **4**(4), 4208–4216, DOI: 10.1021/acsaem.1c00573.

41 W. Bi, J. Huang, M. Wang, E. P. Jahrman, G. T. Seidler, J. Wang, Y. Wu, G. Gao, G. Wu and G. Cao, V_2O_5-Conductive polymer nanocables with built-in local electric field derived from interfacial oxygen vacancies for high energy density supercapacitors, *J. Mater. Chem. A*, 2019, **7**(30), 17966–17973, DOI: 10.1039/C9TA04264D.

42 A. G. Tabrizi, N. Arsalani, H. Namazi and I. Ahadzadeh, Vanadium oxide assisted synthesis of polyaniline nanoarrays on graphene oxide sheets and its application in supercapacitors, *J. Electroanal. Chem.*, 2017, **798**, 34–41, DOI: 10.1016/j.jelechem.2017.04.059.

43 W. Lu, S. Yin, X. Wu, Q. Luo, E. Wang, L. Cui and C.-Y. Guo, Aniline–pyrrole copolymers formed on single-walled carbon nanotubes with enhanced thermoelectric performance, *J. Mater. Chem. C*, 2021, **9**(8), 2898–2903, DOI: 10.1039/D0TC05757F.

44 Y. Wang, W.-B. Ma, L. Guo, X.-Z. Song, X.-Y. Tao, L.-T. Guo, H.-L. Fan, Z.-S. Liu, Y.-B. Zhu and X.-Y. Wei, Phytic acid-doped poly(aniline-co-pyrrole) copolymers for supercapacitor electrodes applications, *J. Mater. Sci.: Mater. Electronics*, 2020, **31**, 6263–6273, DOI: 10.1007/s10854-020-03181-5.

45 L. Sun, D. Chen, S. Wan and Z. Yu, Adsorption studies of dimetridazole and metronidazole onto biochar derived from sugarcane bagasse: kinetic, equilibrium, and mechanisms, *J. Polym. Environ.*, 2018, **26**, 765–777, DOI: 10.1007/s10924-017-0986-5.

46 N. Labbé, D. Harper, T. Rials and T. Elder, Chemical structure of wood charcoal by infrared spectroscopy and multivariate analysis, *J. Agricult. Food Chem.*, 2006, **54**(10), 3492–3497, DOI: 10.1021/jf053062n.

47 B. Li, D. Liu, D. Lin, X. Xie, S. Wang, H. Xu, J. Wang, Y. Huang, S. Zhang and X. Hu, Changes in biochar functional groups and its reactivity after volatile-char interactions during biomass pyrolysis, *Energy Fuels*, 2020, **34**(11), 14291–14299, DOI: 10.1021/acs.energyfuels.0c03243.

48 C. Zhou, J. Han, G. Song and R. Guo, Fabrication of poly(aniline-co-pyrrole) hollow nanospheres with Triton X-100 micelles as templates, *J. Polym. Sci. Part A: Polym. Chem.*, 2008, **46**(11), 3563–3572, DOI: 10.1002/pola.22695.

49 D. Lv, W. Shen, W. Chen, Y. Wang, R. Tan, M. Zhao and W. Song, Emerging poly(aniline co-pyrrole) nanocomposites by in-situ polymerized for high-performance flexible ammonia sensor, *Sens. Actuat. A: Phys.*, 2023, **349**, 114078, DOI: 10.1016/j.sna.2022.114078.

50 M. J. Antony and M. Jayakannan, Role of anionic micellar template on the morphology, solid-state ordering, and unusual conductivity trend in poly(aniline-co-pyrrole) nanomaterials, *J. Phys. Chem. B*, 2011, **115**(20), 6427–6436, DOI: 10.1021/jp2015726.

51 Y. S. Thakur, A. D. Acharya and S. Sharma, Reinforcement of V_2O_5 nanoparticle in polyaniline to improve the optical and UV-shielding properties, *Res. Opt.*, 2023, **11**, 100400, DOI: 10.1016/j.rio.2023.100400.

52 R. Rana, R. Bavisotto, K. Hou, N. Hopper and W. T. Tysoe, Surface chemistry at the solid-solid interface; selectivity and activity in mechanochemical reactions on surfaces, *Chem.: Methods*, 2021, **1**(7), 340–349, DOI: 10.1002/cmtd.202100052.

53 N. Kaliyan and R. V. Morey, Natural binders and solid bridge type binding mechanisms in briquettes and pellets made from corn stover and switchgrass, *Biores. Technol.*, 2010, **101**(3), 1082–1090, DOI: 10.1016/j.biortech.2009.08.064.

54 I. J. Tadeo, R. Parasuraman, S. B. Krupanidhi and A. M. Umarji, Enhanced humidity responsive ultrasonically nebulised V_2O_5 thin films, *Nano Express*, 2020, **11**, 010005, DOI: 10.1088/2632-959X/ab779a.

55 F. Liu, Z. Chen, G. Fang, Z. Wang, Y. Cai, B. Tang, J. Zhou and S. Liang, V_2O_5 nanospheres with mixed vanadium valences as high electrochemically active aqueous zinc-ion battery cathode, *Nano-Micro Lett.*, 2019, **11**, 1–11, DOI: 10.1049/mnl.2015.0108.

56 F. A. Stevie and C. L. Donley, Introduction to X-ray photoelectron spectroscopy, *J. Vac. Sci. Technol. A*, 2020, **38**(6), 063204, DOI: 10.1116/6.0000412.

57 Z. Wang, L. Gao, S. Chen, L. Zhang and X. Yang, V_2O_5/rGO arrays as potential anode materials for high performance sodium ion batteries, *J. Solid State Electrochem.*, 2021, **25**, 721–729, DOI: 10.1007/s10008-020-04844-3.

58 C. Drosos, C. Jia, S. Mathew, R. G. Plagrave, B. Moss, A. Kafizas and D. Vernardou, Aerosol-assisted chemical vapor deposition of V_2O_5 cathodes with high-rate capabilities for magnesium-ion batteries, *J. Power Sour.*, 2018, **384**, 355–359, DOI: 10.1016/j.jpowsour.2018.02.074.

59 K. D. Rasamani, F. Alimohammadi and Y. Sun, Interlayer-expanded MoS_2, *Mater. Today*, 2017, **20**(2), 83–91, DOI: 10.1016/j.mattod.2016.10.004.

60 J.-H. Lin, The influence of the interlayer distance on the performance of thermally reduced graphene oxide supercapacitors, *Materials*, 2018, **11**(2), 263, DOI: 10.3390/ma11020263.

61 B. Liu, H. Sun, T. Peng and X. Zhi, 3D core-shell poly(aniline-co-pyrrole)/reduced graphene oxide composite for supercapacitor performance, *Diamond Related Mater.*, 2021, **118**, 108498, DOI: 10.1016/j.diamond.2021.108498.

62 J. Wang, X. Zhang, Y. Zhang, A. Abas, X. Zhao, Z. Yang, Q. Su, W. Lan and E. Xie, Lightweight, interconnected VO_2 nanoflowers hydrothermally grown on 3D graphene networks for wide-voltage-window supercapacitors, *RSC Adv.*, 2017, **7**(56), 35558–35564, DOI: 10.1039/C7RA04376G.

63 H. Han and S. Cho, Ex situ fabrication of polypyrrole-coated core-shell nanoparticles for high-performance coin cell supercapacitor, *Nanomaterials*, 2018, **8**(9), 726, DOI: 10.3390/nano8090726.

64 L. S. Kuznetsova, V. A. Arlyapov, Y. V. Plekhanova, S. E. Tarasov, A. S. Kharkova, E. A. Saverina and A. N. Reshetilov, Conductive polymers and their nanocomposites: application features in biosensors and biofuel cells, *Polymers*, 2023, **15**(18), 3783, DOI: 10.3390/polym15183783.

65 Y. Liang, Z. Wei, X. Zhang and R. Wang, Fabrication of vanadium oxide@polypyyrole (V_2O_5@PPy) core-shell nanofiber electrode for supercapacitor, *ES Energy Environ.*, 2022, **18**, 101–110, DOI: 10.30919/esee8c783.

66 M. Gale, T. Nguyen, M. Moreno and K. L. Gilliard-AbdulAziz, Physiochemical properties of biochar and activated carbon from biomass residue: influence of process conditions to adsorbent properties, *ACS Omega*, 2021, **6**(15), 10224–10233, DOI: 10.1021/acsomega.1c00530.

67 S. Wu, C. Liu, D. A. Dinh, K. S. Hui, K. N. Hui, J. M. Yun and K. H. Kim, Three-dimensional self-standing and conductive $MnCO_3$@Graphene/CNT networks for flexible asymmetric supercapacitors, *ACS Sustainable Chem. Eng.*, 2019, **7**(11), 9763–9770, DOI: 10.1021/acssuschemeng.8b05935.

68 S. Wang, M. Mao, Y. Cao, H. Luo, H. Wang and D. Guo, Novel cuboid-like cobalt nickel phosphate/manganese dioxide/multi-walled carbon nanotubes composites as binder-free electrodes for high-performance supercapacitors, *Inorg. Chem. Commun.*, 2020, **114**, 107822, DOI: 10.1016/j.inoche.2020.107822.

69 H. Gao, F. Wu, X. Wang, C. Hao and C. Ge, Preparation of $NiMoO_4$-PANI core-shell nanocomposite for the high-performance all-solid-state asymmetric supercapacitor, *Int. J. Hydrogen Energy*, 2018, **43**(39), 18349–18362, DOI: 10.1016/j.ijhydene.2018.08.018.

70 Q. Wu, T. He, Y. Zhang, J. Zhang, Z. Wang, Y. Liu, L. Zhao, Y. Wu and F. Ran, Cyclic stability of supercapacitors: materials, energy storage mechanism, test methods, and device, *J. Mater. Chem. A*, 2021, **9**(43), 24094–24147, DOI: 10.1039/D1TA06815F.

71 C. Pan, H. Gu and L. Dong, Synthesis and electrochemical performance of polyaniline@MnO_2/graphene ternary composites for electrochemical supercapacitors, *J. Power Sour.*, 2016, **303**, 175–181, DOI: 10.1016/j.jpowsour.2015.11.002.

72 H. Gul, A.-H. A. Shah and S. Bilal, Achieving ultrahigh cycling stability and extended potential window for supercapacitors through asymmetric combination of conductive polymer nanocomposite and activated carbon, *Polymers*, 2019, **11**(10), 1678, DOI: 10.3390/polym11101678.

73 B. Pandit, D. P. Dubal, P. Gómez-Romero, B. B. Kale and B. R. Sankapal, V_2O_5 encapsulated MWCNTs in 2D surface architecture: complete solid-state bendable highly stabilized energy efficient supercapacitor device, *Sci. Rep.*, 2017, **7**(1), 43430, DOI: 10.1038/srep43430.

74 M. S. Khan, I. Murtaza, A. Shuja, H. R. Khan, S. Fahad, M. W. Khan, J. Ahmmad, S. M. Wabaidur and M. Z. Ansari, Energy on-the-Go: V_2O_5-pBOA-Graphene nanocomposite for wearable supercapacitor applications, *Electrochim. Acta*, 2024, **486**, 144119, DOI: 10.1016/j.electacta.2024.144119.

75 Z. Liu, H. Zhang, Q. Yang and Y. Chen, Graphene/V_2O_5 hybrid electrode for an asymmetric supercapacitor with high energy density in an organic electrolyte, *Electrochim. Acta*, 2018, **287**, 149–157, DOI: 10.1016/j.electacta.2018.04.212.

76 A. Huang, M. F. El-Kady, X. Chang, M. Anderson, C.-W. Lin, C. L. Turner and R. B. Kaner, Facile fabrication of multivalent VO_x/Graphene nanocomposite electrodes for high-energy-density symmetric supercapacitors, *Adv. Energy Mater.*, 2021, **11**(26), 2100768, DOI: 10.1002/aenm.202100768.

77 D. H. Nagaraju, Q. Wang, P. Beaujuge and H. N. Alshareef, Two-dimensional heterostructures of V_2O_5 and reduced graphene oxide as electrodes for high energy density asymmetric supercapacitors, *J. Mater. Chem. A*, 2014, **2**(40), 17146–17152, DOI: 10.1039/C4TA03731F.

78 M.-H. Bai, T.-Y. Liu, F. Luan, Y. Li and X.-X. Liu, Electrodeposition of vanadium oxide–polyaniline composite nanowire electrodes for high energy density supercapacitors, *J. Mater. Chem. A*, 2014, **2**(28), 10882–10888, DOI: 10.1039/C3TA15391F.

79 A. Aamir, A. Ahmad, S. K. Shah, N. Ain, M. Mehmood, Y. Khan and Z. Rehman, Electro-codeposition of V_2O_5-polyaniline composite on Ni foam as an electrode for supercapacitor, *J. Mater. Sci.: Mater. Electronics*, 2020, **31**(23), 21035–21045, DOI: 10.1007/s10854-020-04616-9.

80 M. Li, G. Sun, P. Yin, C. Ruan and K. Ai, Controlling the formation of rodlike V_2O_5 nanocrystals on reduced graphene oxide for high-performance supercapacitors, *ACS Appl. Mater. Interfaces*, 2013, **5**(21), 11462–11470, DOI: 10.1021/am403739g.